RESEARCH ARTICLE

A Control Bandwidth Optimized Active Damping Scheme for LC and LCL Filter-Based Converters

WENYONG GUO [1], (Member, IEEE), **TIANXIANG CHEN** [2], (Member, IEEE), **AND ALEX Q. HUANG** [2], (Fellow, IEEE)

[1]School of Electrical Engineering, Beijing Jiaotong University, Beijing 100044, China
[2]Chandra Department of Electrical and Computer Engineering, The University of Texas at Austin, Austin, TX 78712, USA

Corresponding author: Wenyong Guo (wyguo@bjtu.edu.cn)

ABSTRACT Control bandwidth and damping performance are two key specifications for high-order LC and LCL filter-based converters. The damping of high-order filter-based converters has been extensively studied. However, the control bandwidth issue was ignored. The quantitative relationship between the control gains and bandwidth is still unclear. Moreover, the delay compensator was designed independently without considering the interactions with the main controller. This paper proposes a control bandwidth-optimized active damping control strategy for the LC and LCL filter-based converters to overcome these shortcomings. With the proposed generalized controller, the close loop transfer function of the Nth order filter-based converter can be simplified to an Nth order low pass filter with an adjustable cutoff frequency. This greatly simplifies the control bandwidth optimization. To alleviate the negative influence of the computational delay on the control bandwidth, a novel delay compensator is proposed. To reach an overall optimized control performance, the particle swarm optimization (PSO) method is used to optimize the controller and delay compensator parameters simultaneously to realize both high control bandwidth and good damping performance. Experimental results verify the effectiveness of the proposed novel controller.

INDEX TERMS Active damping, current source converter, LC filter, LCL filter, optimal control, three-phase converter, voltage source converter.

I. INTRODUCTION

Power converters generate high-frequency switching harmonics. To filter out the switching harmonics, filters are needed. First-order L or third-order LCL filters are typically used to interface the voltage source converter (VSC) with the grid. Compared with the L filter, the LCL filter has the advantage of smaller size and lower cost [1] and is more widely used. A second-order LC filter is also widely used in the current source converter (CSC) or VSC. In the CSC, the LC filter is used to filter out the current harmonics and is typically used to interface with the grid to realize bidirectional power flow control [2]. In the case of a VSC, an LC filter is used to filter out the switching ripple and output a controllable and high-quality voltage source. This is widely used in the motor

drive [3], dynamic voltage restorer [4], and uninterruptable power supply [5].

Resonance is a major problem with high-order filters such as the LC and LCL filters. To solve this problem, numerous damping solutions have been proposed.

Passive damping (PD) with damping resistors is the simplest way to solve the problem. The resistor can be connected in parallel with the inductor to improve the damping of the LC filter. The PD makes the control system of the LCL filter-based VSC simple [6]. However, additional power losses are introduced. A thorough investigation of the PD for the LCL filter is presented in [7]. As analyzed in [7], a composite passive damper composed of paralleled RC and RL dampers is needed to adapt to both weak and stiff grid conditions. To minimize the power losses, the critical damping ratio is studied to flatten the LCL filter resonant peak without introducing unnecessary losses [8].

The associate editor coordinating the review of this manuscript and approving it for publication was Fengjiang Wu [ID].

Active damping (AD) is also widely used to damp the resonance of the LCL filter. Various filter variables have been utilized to damp the resonance.

Filter capacitor current is typically used to damp the resonance [9], [10], [11], [12]. The capacitor current active damping is equivalent to passive resistor damping with resistors connected in series with the capacitor if a second-order high pass filter is used [10]. Capacitor current proportional-integral (PI) positive feedback AD can ensure a positive equivalent resistance within the Nyquist frequency [11].

The capacitor voltage is also an effective variable that can be used to damp the LCL filter resonance. It was demonstrated that a derivative compensator was usually necessary to realize AD [13]. To overcome the shortcoming of direct derivative discretization, which results in large phase error and amplifies high-frequency noise, various discretization methods were proposed, including lead-lag compensator [14], high pass filter [15], nonideal generalized integrator [16], [17], and digital notch filter [18]. It is also found out that the LCL filter resonance can also be damped by the proportional and second-order derivative of the capacitor voltage [19].

Grid side current ADs are preferred by some authors since it helps the direct control of the output current without additional sensors. It can be implemented by the feedback of the second-order [20] or the first-order differential of the grid current [21].

Inverter side current can also be used for AD. It was identified that the inverter side current AD can suppress the resonance peak well with a smaller resonance frequency offset and maintain a high-power quality compared with the grid-side current active damping method [22]. It is also found that the inverter current feedback is equivalent to adding a resistor in series with the inverter side inductor. Therefore, the inverter current can be used alone to damp the resonance [23].

In addition to these filter variable AD controls, feedforward of the point of common coupling (PCC) voltage is used to provide an inherent AD [24]. The combinations of different variables are also studied to further improve the AD performance. A hybrid AD that combines the capacitor current feedback and PCC voltage feedforward was proposed in [25], which ensures the positive damping range could cover the entire frequency spectrum.

Observer-based AD was also proposed, which estimates the unmeasured LCL filter states for the AD. LCL filter capacitor current is estimated by the observer and used for the AD in [26]. Good damping performance is achieved by the proper selection of observer poles and damping gains. Luenberger observer-based active damping was presented in [27]. All frequencies' passive output admittance of the inverter can be achieved with proper parameter design. A thorough investigation of the different observer structure designs and control output settings was presented in [28]. Robustness in weak grid conditions was verified.

Hybrid AD and PD schemes have also been investigated [29]. The AD is based on grid current feedback, which

reduces the mid-frequency non-passive region. The PD is realized by connecting a resistor in series with the capacitor, which improves the high-frequency performance.

The delay caused by the digital controller is another key factor that influences the performance of the AD. The AD performance deteriorates due to the negative equivalent resistance caused by the digital control delay. To overcome this shortcoming, various delay compensation methods were proposed and can be generally classified into two major categories: the model-based ones and the model-free alternatives. The model-based ones calculate the variables ahead of time based on difference equations [30]. It is therefore very dependent on the model accuracy.

To address this issue, model-free methods were proposed. Early proposals utilized linear extrapolation to predict forthcoming control values [31]. To improve the compensation effect at higher frequencies, digital filter-based compensation methods were further introduced. A first-order filter based delay compensation approach was proposed in [32], which extends the damping region from 1/6 to 1/4 of the sampling frequency. To avoid an infinite gain at the Nyquist frequency, a modified first-order filter was proposed to reach a compromise between the phase compensation and noise attenuation [33]. A second-order generalized integrator was applied to provide a phase lead with a limited gain near the Nyquist frequency by tuning the damping term [34]. An improved time-delay compensation approach is proposed based on additional area insertion (AAI), which widens the phase compensation frequency [35]. A delay compensator dedicated to eliminate the delay in the AD loop is presented in [36]. With the proposed compensator, the influence of delay on damping performance can be eliminated. However, the influence on the control bandwidth hasn't been considered.

Although various damping methods have been proposed in the literature as summarized above, other key issues, such as the control bandwidth, have not been considered. The control bandwidth is the most important parameter in some applications such as dynamic voltage restorers, active power filters, and future grid-forming inverters. To maximize the control bandwidth while maintaining good damping performance at the same time, an optimization approach is needed. Another important factor that influences the bandwidth is the computational delay. Although various delay compensation methods have been proposed, the parameters of the delay compensator were predetermined and not co-optimized with the control parameters.

To extend the control bandwidth as high as possible while maintaining a good damping performance and a high stability margin, a control bandwidth optimized AD control method for the LC and LCL filter based converters is proposed in this paper. The novelties of this paper are:

A. A CONTROL BANDWIDTH OPTIMIZED ACTIVE DAMPING SCHEME IS PROPOSED

With the proposed control scheme, the closed-loop transfer function can be simplified to an Nth order filter (where N is

equal to the filter order) with an adjustable cut-off frequency to tune the control bandwidth. The steady-state performance can be tuned by the pole introduced by the integrator. The proposed control enables for the first time a clear optimization methodology to tune both the dynamic and steady-state controller performance.

B. A NOVEL DELAY COMPENSATOR IS PROPOSED
To counteract the negative influence of the computational delay, a novel delay compensator with excellent performance is proposed. The proposed delay compensator has a better high-frequency response than the conventional ones, which makes it have better delay compensation performance.

C. A GLOBAL OPTIMIZATION SCHEME IS PROPOSED
To reach a global optimal control performance, a global optimization scheme, which takes cut-off frequency, integrator-introduced pole value, computational delay parameters, and differentiation parameters into account, is proposed to maximize the control bandwidth while ensuring good damping performance. A novel cost function, which considers bandwidth and phase error, is also proposed. Good dynamic performance is verified.

This paper is arranged as follows: the control bandwidth optimal damping control method for LC and LCL filter based converters is presented in Section II; A novel delay compensator is presented and analyzed in Section III; Global optimization and its detailed implementations are presented in Section IV; Control system design results are presented in Section V; Experimental results are shown in Section VI to verify the performance of the control strategy; Conclusions are drawn in Section VII.

II. GENERALIZED CONTROL IN CONTINUOUS DOMAIN
The topology of a VSC with various filter configurations is shown in Fig.1. The converter is connected to the grid with an LCL filter. The converter can also be used as a power supply for the load with an LC filter.

A. CONTROL FOR SECOND-ORDER LC FILTER-BASED VSCs
The differential equations for the VSC with an LC filter can be expressed in the complex form as:

$$
\begin{bmatrix} \dfrac{di_L}{dt} \\ \dfrac{du_c}{dt} \end{bmatrix}
= \begin{bmatrix} -j\omega - \dfrac{R_f}{L_f} & -\dfrac{1}{L_f} \\ \dfrac{1}{C_f} & -j\omega \end{bmatrix}
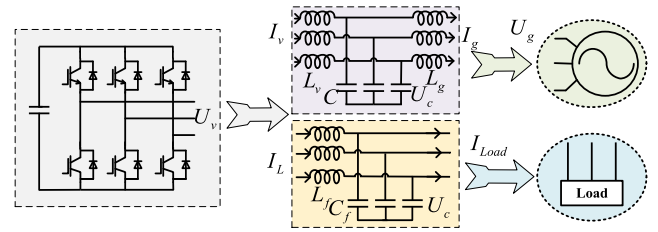\begin{bmatrix} i_L \\ u_c \end{bmatrix}
$$

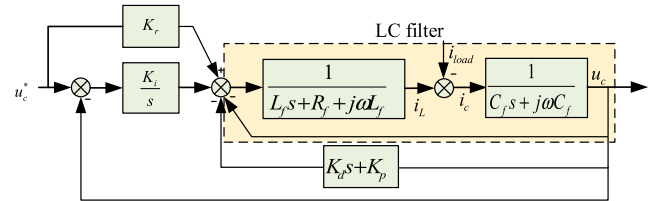**FIGURE 1.** Topology of VSC with different types of AC side filters.

FIGURE 2. Control block diagram for the LC filter-based converter.

$$
+ \begin{bmatrix} \dfrac{1}{L_f} & 0 \\ 0 & -\dfrac{1}{C_f} \end{bmatrix}
\begin{bmatrix} u_v \\ i_{load} \end{bmatrix} \tag{1}
$$

where R_f, L_f, and C_f are resistance and inductance of the inductor and capacitance of the capacitor, i_c and i_L are the capacitor and inductor current, u_c is the capacitor voltage, u_v is the inverter voltage, i_{load} is the load current, ω is the grid angular frequency. To control the output voltage u_c, a single variable control scheme with both feedforward and feedback terms is proposed with its control block diagram shown in Fig.2. where u_c^* and u_c are the capacitor reference and measured voltage, K_r, K_p, K_d, and K_i are the feedforward, proportional, differential, and integrator gains respectively.

The part encircled in the dashed line is the physical model of the LC filter. The feedforward controller adds one zero (z) in the close loop, while the integrator adds one pole (p) in the close loop. The transfer function from U_c^* to U_c is expressed in Eq. (2), as shown at the bottom of the page.

$G_u(s)$ can be rewritten as:

$$
G_u(s) = \frac{\omega_n^2 (s + z_0)}{(s^2 + 2\zeta\omega_n s + \omega_n^2)(s + p)} \tag{3}
$$

To cancel the influence of the integrator in the close loop, the zero added by the feedforward controller is set to be equal to the pole introduced by the integrator. That is: $z_0 = p = K_i/K_r$.

Eq. (3) can be simplified as:

$$
G_u(s) = \frac{\omega_n^2}{s^2 + 2\zeta\omega_n s + \omega_n^2} \tag{4}
$$

$$
G_u(s) = \frac{K_r s + K_i}{L_f C_f s^3 + (R_f C_f + 2j\omega L_f C_f + K_d)s^2 + (j\omega R_f C_f - \omega^2 L_f C_f + K_p + 1)s + K_i} \tag{2}
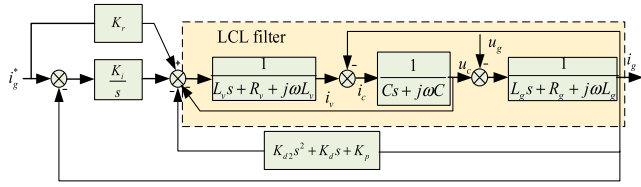$$

FIGURE 3. Control block diagram for the LCL filter-based converter.

That is:

$$u_{cd} + ju_{cq} = \frac{\omega_n^2}{s^2 + 2\zeta\omega_n s + \omega_n^2} \times (u_{cd}^* + ju_{cq}^*) \quad (5)$$

Expressed in the matrix form, we have:

$$\begin{bmatrix} u_{cd} \\ u_{cq} \end{bmatrix} = \begin{bmatrix} \dfrac{\omega_n^2}{s^2 + 2\zeta\omega_n s + \omega_n^2} & 0 \\ 0 & \dfrac{\omega_n^2}{s^2 + 2\zeta\omega_n s + \omega_n^2} \end{bmatrix} \begin{bmatrix} u_{cd}^* \\ u_{cq}^* \end{bmatrix} \quad (6)$$

Natural decoupling between the dq axis can also be verified through Eq. (6) since the cross-coupling terms are zero.

As it can be seen from Eq.(6), the close loop is a second-order system, the damping performance is determined by the damping factor ζ. The damping factor ζ needs to be properly selected to ensure good damping performance. Selecting $\zeta = 0.707$, the second-order system G_u has the highest dynamic performance, and the corresponding bandwidth is ω_n.

Comparing Eq. (2) with Eq. (3), we can get:

$$K_r = \omega_n^2 L_f C_f \quad (7)$$
$$K_i = K_r p \quad (8)$$
$$K_d = 2\zeta\omega_n L_f C_f + p_2 L_f C_f - R_f C_f - 2j\omega L_f C_f \quad (9)$$
$$K_p = (\omega_n^2 + \omega^2)L_f C_f + 2\zeta p\omega_n L_f C_f - j\omega R_f C_f - 1 \quad (10)$$

From Eq. (8), it is can be found out that the integrator coefficient K_i is proportional to p, which demonstrates that p influences the steady-state performance. Since L_f, C_f, R_f, ω, and ζ are all known parameters, the only parameters that influence the control gains are ω_n and p. ω_n determines the bandwidth of the close loop system, while p is the pole introduced by the integrator which determines the steady state performance. Therefore, both dynamic and steady state performance can be tuned by adjusting ω_n and p independently, which makes it flexible to tune the system performance.

B. CONTROL FOR THIRD-ORDER LCL FILTER-BASED VSCs
Similarly, a single variable control scheme with both feedforward and feedback terms can also be applied to the LCL filter base VSC. The control block diagram is shown in Fig.3.

where I_g^* is converter reference grid side voltage, K_r, K_p, K_d, K_{d2}, and K_i are the feedforward, proportional, differential, second-order differential, and integrator gain respectively. The part encircled in the dashed line is the physical model of the LCL filter.

The transfer function from I_g^* to I_g can be derived as (11), shown at the bottom of the page.

$G_i(s)$ can be rewritten as:

$$G_i(s) = \frac{\omega_n^2 p_1(s + z_0)}{(s^2 + 2\zeta\omega_n s + \omega_n^2)(s + p)(s + p_1)} \quad (12)$$

To cancel the influence of the integrator, z_0 is also set to be equal to p. Eq. (12) can be simplified as:

$$G_i(s) = \frac{\omega_n^2 p_1}{(s^2 + 2\zeta\omega_n s + \omega_n^2)(s + p_1)} \quad (13)$$

$G_i(s)$ can be regarded as a first-order system connected in series with a second-order system. The first order system has only one real pole without imaginary part, which doesn't induce resonance. Only the damping factor ζ of the second order system need to be carefully design to avoid resonance. ζ is also selected as 0.707 to make the second-order system have the fastest dynamic response. The bandwidth of the first order and second-order systems are ω_n and p_1 respectively. To make it easy to tune the bandwidth of the whole system, p_1 is selected to be equal to ω_n. The multiplication of two filters with the same cutoff frequency yields a higher-order filter with the same cutoff frequency. Since the cutoff frequency of the first and second-order filters are both ω_n, the bandwidth of $G_i(s)$ is therefore also ω_n. $G_i(s)$ can therefore be modified as:

$$G_i(s) = \frac{\omega_n^3}{(s^2 + 2\zeta\omega_n s + \omega_n^2)(s + \omega_n)} \quad (14)$$

where $\omega_n = \sqrt[3]{K_r/L_g L_v C}$
That is:

$$i_{gd} + ji_{gq} = \frac{\omega_n^3}{(s^2 + 2\zeta\omega_n s + \omega_n^2)(s + \omega_n)} \times (i_{gd}^* + ji_{gq}^*) \quad (15)$$

Expressed in the matrix form, Eq. (16) can be derived, as shown at the bottom of the next page. The cross-coupling term in Eq. (16) is also zero, which verifies the decoupling of dq axes.

Comparing Eq. (11) with Eq. (12), we can get the detailed values of control gains, which is shown in (17-21):

$$K_r = \omega_n^3 L_g L_v C \quad (17)$$
$$K_i = K_r p \quad (18)$$
$$K_{d2} = pL_g L_v C + (1 + 2\zeta)\omega_n L_g L_v C - R_g L_v C - R_v L_g C - 3j\omega L_v L_g C \quad (19)$$

$$G_i(s) = \frac{K_r s + K_i}{L_g L_v C s^4 + (R_g L_v C + R_v L_g C + K_{d2})s^3 + (L_v + L_g + R_g R_v C + K_d)s^2 + (K_p + R_g + R_v)s + K_i} \quad (11)$$
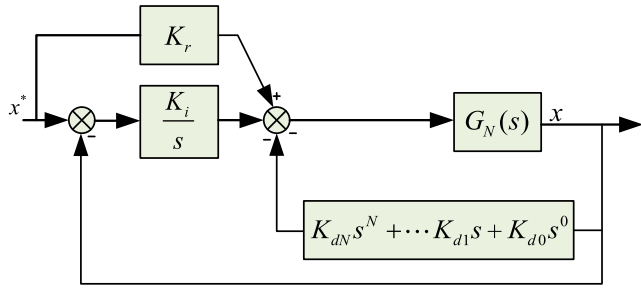
FIGURE 4. Generalized Control block diagram for the Nth order filter based converter.

$$
\begin{aligned}
K_d ={}& 3L_g L_v C\omega^2 - L_v - R_g R_v C - L_g + L_g L_v C\omega_n^2 \\
& - 2j\omega L_g R_v C - 2j\omega L_v R_g C + L_g L_v Cp_3\omega_n \\
& + 2\zeta L_g L_v C\omega_n^2 + 2\zeta L_g L_v Cp\omega_n
\end{aligned}
\tag{20}
$$

$$
\begin{aligned}
K_p ={}& L_g L_v C(\omega_n^3 + j\omega^3) + (R_g L_v + R_v L_g)C\omega^2 - jR_g R_v C\omega \\
& - (R_v + R_g) - j(L_g + L_v)\omega + 2\zeta L_g L_v Cp\omega_n^2 \\
& + L_g L_v Cp\omega_n^2
\end{aligned}
\tag{21}
$$

From Eq. (17-21), it can also be found out that the control parameters can be adjusted by varying ω_n and p, which makes it flexible to tune both the dynamic and steady state performance.

C. GENERALIZATION OF THE CONTROLLER FOR NTH ORDER FILTER-BASED CONVERTER

To summarize, the proposed control scheme can be generalized. As shown in Fig.4, the generalized controller is composed of feedforward, integration, and feedback terms.

The same control structure can be used in the feedforward and integration terms with any order filter. The feedback terms are changed with the order of the filter. For the single variable feedback controller, 0 to $(N-1)^{th}$ order derivative feedback terms are used for the Nth order filter-based converter. The general expression of the simplified closed-loop control transfer function can be expressed as:

$$
G_N(s) =
\begin{cases}
\dfrac{\omega_n^N}{(s^2 + 2\zeta\omega_n s + \omega_n^2)^{N/2}}, & even \\[12pt]
\dfrac{\omega_n^N}{(s^2 + 2\zeta\omega_n s + \omega_n^2)^{(N-1)/2}(s + \omega_n)}, & odd
\end{cases}
\tag{22}
$$

By proper selecting the damping factor ζ, the resonances can be avoided. The performance of the controller is directly related to the two parameters: ω_n and p. ω_n is related to control bandwidth, which determines the dynamic performance;
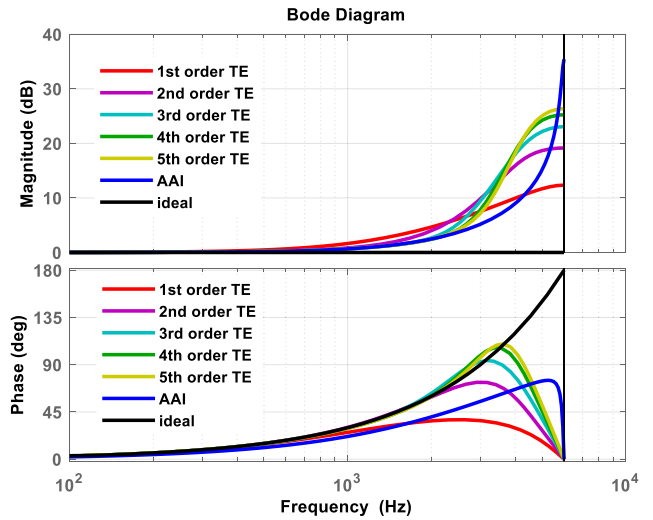

FIGURE 5. Bode diagram comparison between the TP and AAI methods.

while p is related to the integrator gain, which determines the steady-state performance. The advantage of the proposed control strategy is straightforward in expression and easy to tune the parameters. The parameters needed to be tuned are the cut-off frequency ω_n and integrator introduced pole value p, which determine the dynamic and steady-state performance respectively.

D. REALIZATION OF s AND s^2

s and s^2 can be realized by analog or digital differentiators. The analog differentiator can be realized by analog operational amplifiers with chip resistors and capacitors. The Tustin method is usually used as a digital differentiator, which induces noise amplification due to the infinite gain at the Nyquist frequency. To avoid noise amplification at high frequency, a nonideal generalized integrator (GI) [16] is used in this paper to realize digital differentiation. The transfer function of the GI is:

$$
GI(s) = \frac{\omega'^2 s}{s^2 + \omega_c' s + \omega'^2}
\tag{23}
$$

where ω' is Nyquist frequency, ω_c' is the cutoff frequency of GI(s). To realize s^2, two GIs are multiplied. It also needs to note that the GI induces phase shift at the high-frequency range, which is one of the major bottlenecks that influence the performance of the whole control system. Therefore, analog differentiators are suggested to be used if the performance of digital differentiator is unsatisfactory.

$$
\begin{bmatrix} i_{gd} \\ i_{gq} \end{bmatrix} =
\begin{bmatrix}
\dfrac{\omega_n^3}{(s^2 + 2\zeta\omega_n s + \omega_n^2)(s + \omega_n)} & 0 \\[14pt]
0 & \dfrac{\omega_n^3}{(s^2 + 2\zeta\omega_n s + \omega_n^2)(s + \omega_n)}
\end{bmatrix}
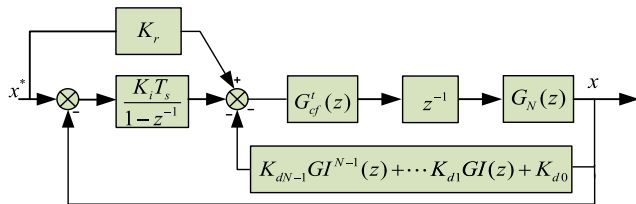\begin{bmatrix} i_{gd}^* \\ i_{gq}^* \end{bmatrix}
\tag{16}
$$

FIGURE 6. Generalized discretized Control block diagram.

III. NOVEL TIME DELAY COMPENSATION METHOD

As analyzed before, the control bandwidth can be infinite without considering the practical converter limits. The dominant physical limit is the control delay. To alleviate the negative influence of the control delay, a simple but effective delay compensation method is proposed in this paper.

The transfer function of the delay is:

$$G_d(s) = e^{-T_d s} \tag{24}$$

To fully compensate the control delay, the ideal delay compensation transfer function is:

$$G_c(s) = e^{T_d s} \tag{25}$$

The Taylor expansion of $G_c(s)$ is:

$$G_c^t(s) = 1 + T_d s + \frac{1}{2!}(T_d s)^2 + \frac{1}{3!}(T_d s)^3 + \cdots \tag{26}$$

As it can be seen from (26), $G_c^t(s)$ contains high order derivatives, which amplifies noise. To suppress the noise, the Nth order filter is connected in series with N^{th} order derivatives. The transfer function of the Taylor expansion after filtering is shown in (27):

$$\begin{aligned} G_{cf}^t(s) = 1 &+ \frac{\omega_c}{s + \omega_c} T_d s + \frac{1}{2} \frac{\omega_c^2}{s^2 + 2\zeta\omega_c + \omega_c^2}(T_d s)^2 \\ &+ \frac{1}{6} \frac{\omega_c}{s + \omega_c} \frac{\omega_c^2}{s^2 + 2\zeta\omega_c + \omega_c^2}(T_d s)^3 + \cdots \end{aligned} \tag{27}$$

where ω_c is the cutoff frequency, $G_{cf}^t(s)$ is in continuous form. To make it applicable, it needs to be transformed into a discrete form. By the trial-and-error method, the Tustin method is identified as the best discretization method.

The additional area insertion (AAI) [35] delay compensation method is an improvement of the filter-based delay compensation methods and has a wider phase compensation frequency compared with existing filter-based methods. It is used here for delay compensation performance comparison. The transfer function of the AAI is:

$$H(z) = \frac{(1 + \alpha + \beta) - \beta z^{-1}}{1 + \alpha z^{-1}} \tag{28}$$

The recommended coefficient values are: $\alpha = 0.95$, $\beta = 0.5$ [35]. Fig.5 is the comparison between the frequency response of the proposed Taylor expansion (TE) method, the AAI method, and ideal compensation. The sampling and cutoff frequencies are 12kHz and 6kHz respectively. The red,

magenta, cyan, green, and yellow lines denote the first, second, third, fourth, and fifth order approximations with Tustin discretized TE method respectively. The blue and black lines denote the frequency response of the AAI and ideal delay compensations respectively.

As it can be seen from Fig.5, the phase responses of the TE method with second-order and above approximations are closer to the ideal compensation than that of the AAI method. The higher the order, the closer the phase approximation. However, high order approximation also results in higher magnitude gain at high frequency, which may amplify the noise. Considering both noise attenuation and computational burden, the second-order approximation is selected. In (27), uniform T_d is used based on the TE method. However, different T_d values can give more freedom of optimization. Therefore, different T_d value is used for different order differential terms. For the Tustin differential method, the pre-warp frequency can be used as another degree of freedom for optimization. Therefore, it is also tuned in the global optimization discussed below.

IV. PARAMETER TUNING AND GLOBAL OPTIMIZATION

In the continuous control strategy derived in Section II, it is assumed that an analog controller and an idea linear power amplifier are used. The delay and digital differential effect have to be taken into account when a digital controller and a pulse width modulation (PWM) converter are used. The delay can be regarded as an additional inner loop behaved like a low pass filter with a cutoff frequency $\omega_d (\omega_d = 2f_s/3$, f_s is the sampling frequency). The proposed controller can be regarded as an outer control loop. The bandwidth of the outer loop is usually designed to $1/10 \sim 1/5$ of the inner loop to avoid interfering with the control dynamics of the inner loop. Therefore ω_n can be selected to be $1/5$ of ω_d without a delay compensator. p can be selected to a relatively large value to guarantee enough safe margin. To further increase the control bandwidth, a delay compensator can be used. However, its gain increases with increasing frequency, which may weaken the stability. The phase shift induced by the digital differentiator at the high-frequency range also limits the bandwidth and weakens the stability. Therefore, both delay compensator and digital differentiator parameters should be co-optimized with controller parameters to maximize the overall performance in a full digitized controller. To make accurate modeling for the digital controller, the whole control system is remodeled in the z domain. The z domain control block diagram for the Nth order filter-based converters is shown in Fig.6, where z^{-1} is the time delay, $G_{cf}^t(z)$ is the discretized TE, and $G_N(z)$ is the discretized controlled plant with zero-order hold discretization method.

From Fig.6, it can be found out that the overall performance of the control system is determined by four factors:

1) the control gains which are determined by the control bandwidth ω_n;
2) integrator introduced pole p;

3) the delay compensator parameters.
4) The digital differentiator parameters, which is the cut-off frequency ω_c' for the GI method.

For the second-order TE delay compensator, four parameters can be tuned: the first and second-order delay compensation time T_{d1} and T_{d2}, low pass filter cutoff frequency ω_c, and pre-warp frequency ω_p used in Tustin discretization.

For LCL filter-based converter, both first order and second derivative feedback terms are needed. To differentiate the first-order derivative term and avoid high-frequency noise amplification, the GI differential method is used and the transfer function is shown in (23). The first order hold discretization method is suggested to discretize GI(s) [16] and is denoted as GI(z). For the second-order derivative term, two GIs are multiplied to realize the second-order differentiation. To have more degrees of freedom for the optimization, different cutoff frequencies are used for the first and second-order GIs and are denoted as ω_{c1}' and ω_{c2}'.

Since all of these parameters influence the control performance, they should be tuned globally to reach an optimal control performance. The particle swamp optimization (PSO) method is hence used to tune the control parameters. The optimization objective is to increase the control bandwidth while maintaining enough stability margin. The bandwidth of a control loop is defined as the frequency at which the closed-loop amplitude response reaches -3 dB, and it cannot reflect the phase information. In order to track the high-frequency reference signals precisely, it requires both the output signal magnitude and phase to be as close to the reference ones as possible. So, a novel cost function is defined as:

$$J = BP_s^{\gamma} \tag{29}$$

$$P_s = \frac{\alpha + \pi}{\pi} \tag{30}$$

where B is the bandwidth of the closed-loop system, P_s is the index of the phase error, and α is the phase shift of the closed-loop system at the bandwidth frequency, which is a negative value. If the phase shift is zero, P_s is 1, which is the largest value. If the phase shift is $-\pi$, P_s is 0, and the output signal is 180^0 out of phase with the original value. Therefore, a smaller phase shift results in a larger P_s. γ is the index that determines the relative influence of bandwidth and phase shift. If γ is one, the bandwidth and phase shift play equal important role in the optimization process. The cost function J can therefore reflect both magnitude and phase tracking performance.

To ensure the closed-loop system has enough stability margin and good damping performance, two updating conditions are set:

1. The minimum real values of all poles are less than -300 in the continuous domain, which means all the poles in the discrete domain are within a circle with a radius of 0.9753(the sampling frequency is 12kHz).
2. The damping performance is ensured by the minimum damping ratio of the dominant poles. Although the damping ratio is set to be 0.707 in the continuous domain, it will deviate from the preset value during

digitalization. The damping ratio of the dominant poles (the poles that are closest to the unit circle) is set to be larger than 0.7, which is used to ensure a good damping performance.

To implement the PSO algorithm, both personal and global best positions (P_{Pbest} and P_{Gbest}) are used to update each particle's velocity so as to direct them into better regions. The flowchart of the PSO is shown in Fig. 7, which is explained as follows:

Set initial velocity V and position P (ω_n, p, T_{d1}, T_{d2}, ω_p, ω_c, ω_{c1}', ω_{c2}') of each particle.

1) Use the position value to calculate the control gains, delay compensation, and digital differentiation parameters so as to get the system's closed-loop transfer function. Calculate the cost function J based on the closed-loop transfer function in MATLAB.
2) Check whether the two updating conditions are satisfied. If satisfied, compare the J value of each particle with its personal best value (J_{Pb}) and global best value (J_{Gb}). Update the J_{Pb}, J_{Gb}, P_{Pbest}, and P_{Gbest} if the following rules are satisfied:
   - If $J > J_{Pb}$, then $J_{Pb} = J$, $P_{Pbest} = P$
   - If $J_{Pb} > J_{Gb}$, then $J_{Gb} = J_{Pb}$, $P_{Gbest} = P_{Pbest}$
3) Update the particle velocity and position with the particle swamp rules:

$$V_i = V_i + c_1 * \text{rand}() * (P_{Pbest}i - P_i) + c_2$$
$$* \text{rand}() * (P_{Gbest}i - P_i) \tag{31}$$
$$P_i = P_i + V_i \tag{32}$$

where V_i and P_i are velocity and position of each particle, c_1 and c_2 are the learning factors, rand() is the random number between 0 and 1 respectively.
4) Check the stopping criterion. If the number of the iteration has reached the preset value, the PSO procedure is stopped. Otherwise, return to step 2 to repeat the optimization.
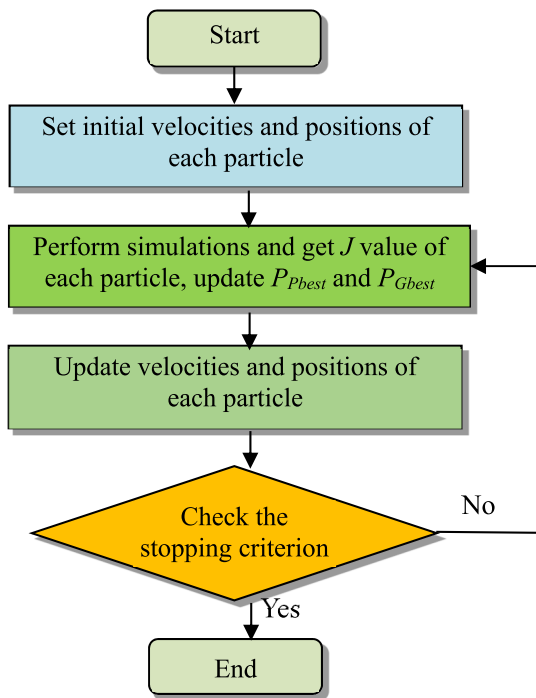
V. EXPERIMENTAL SETUP AND DESIGN EXAMPLES

To verify the effectiveness of the proposed controller and optimization approach, an experimental platform with two VSCs connected with LC and LCL filters is developed, which is shown in Fig.8. The detailed setup parameters are listed in Table 1. The VSCs are commercial IGBT converters from Semikron. Double edge sampling is used, i.e. the modulation index is updated at both upper and lower tips of the triangular carrier, which enables the sampling frequency to be twice as much as that of the switching frequency.

For comparison, the control parameters with the AAI delay compensation method are also optimized by the PSO. Fig.9 is the bode diagram of the closed-loop system of $G_u(s)$ of the LC filter-based converter with the designed control and LC filter parameters. To compare the delay compensation performance, the bode diagrams of the close-loop system using TE and AAI are shown in the same figure. The parameters of the

TABLE 1. Control parameters for the LC filter based converters.

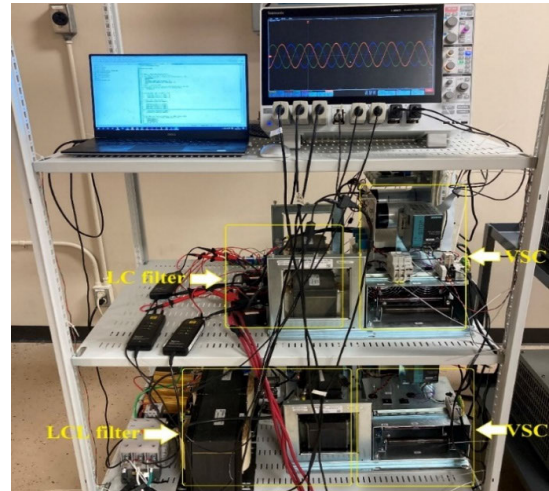| Symbol	Quantity	Value
f	sampling frequency	12kHz
f_s	switching frequency	6kHz
L	LC filter inductor inductance	765μH
R	LC filter inductor resistance	8$m\Omega$
C	LC filter capacitor capacitance	44μF
L_g	LCL filter grid side inductor inductance	2.5mH
R_g	LCL filter grid side inductor resistance	54$m\Omega$
C_f	LCL filter capacitor capacitance	6μF
L_v	LCL filter grid side inductor inductance	2.5mH
R_v	LCL filter grid side inductor resistance	53$m\Omega$
C_{dc}	DC link capacitance	1680μH

FIGURE 7. The optimization flowchart based on PSO.

FIGURE 8. Experimental Setup with LC and LCL filter-based VSCs.

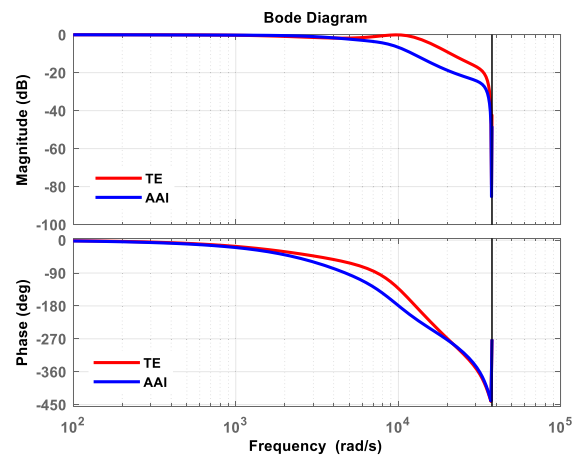**FIGURE 9.** Bode diagram of Gu(s) of the LC filter-based converter.

AAI are also tuned in the same way as the TE by using the proposed global optimization method.

In Fig.9, the red and blue lines are the frequency response with the TE and AAI methods respectively. From Fig.9, it is clear that the control bandwidth with the TE is much higher than that of the AAI, while the phase shift with the TE is much smaller than that of the AAI method. The bandwidths with TE and AAI are 6321rad/s and 4040rad/s respectively. The phase shift with TE and AAI at the bandwidth frequency are 76° and 78° respectively. The control performance with the TE method is therefore much better than that of the AAI.

Fig.10 is the bode diagram of the closed-loop system of Gi(s) of the LCL filter-based converter. The red and blue lines are the frequency response with the TE and AAI methods respectively. From Fig10, it can be seen that the magnitude with the TE is higher than that of the AAI at a high-frequency range, while the phase shift with the TE is smaller than that of the AAI method. The bandwidths with TE and AAI are 2611rad/s and 2583rad/s respectively. The phase shift with TE and AAI at the bandwidth frequency are 61° and 76° respectively. Compared with the LC filter-based converter, the control performance with the TE method is also better than that of the AAI. The performance difference is not so significant with the TE and AAI methods. This is due to that the GI introduces phase shift and magnitude amplification in the high-frequency range. The second-order derivative feedback term is needed for the LCL filter-based converter, which necessitates the multiplication of two GIs and causes twice phase shift. So, the phase shift induced by the GI is the bottleneck that degrades the closed-loop performance with the digital differentiator. To break the bottleneck, analog differentiators can be used. The analog differentiators are not used here to save the cost since the performance is already satisfactory.

VI. EXPERIMENTAL RESULTS
To verify the effectiveness of the proposed controller and optimization approach, experiments for the LC and LCL filter-based converters have been carried out.
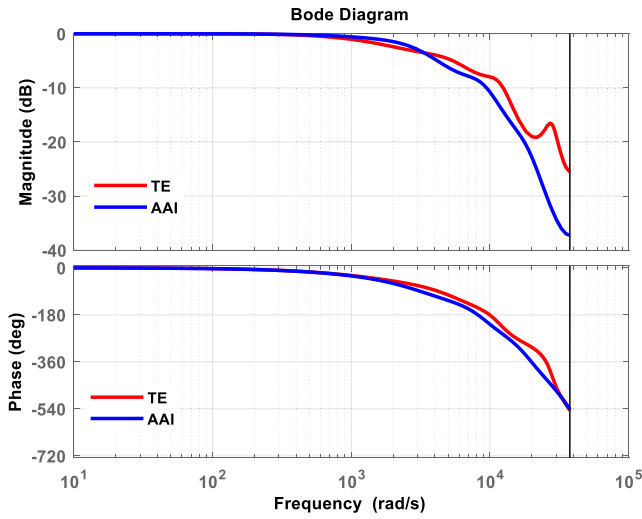
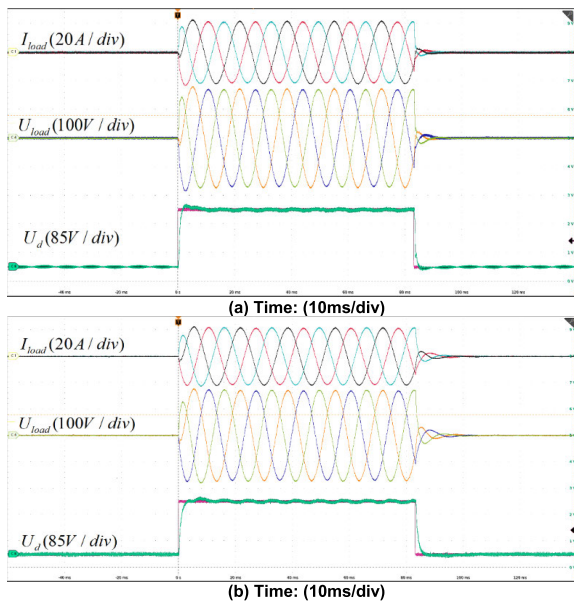**FIGURE 10.** Bode diagram of Gi(s) of the LC filter-based converter.

FIGURE 11. Step response of the LC filter-based converter: (a) with the TE (b) with AAI delay compensation method.

Fig.11 is the step response results of the LC filter-based converter with the TE and AAI delay compensation method respectively. The converter is controlled in the *dq* reference frame. The *q* reference is kept zero, the *d* reference RMS voltage is changed from 0V to 120V periodically. From top to bottom, the three waveforms are load current, load voltage, *d* reference, and measured voltage respectively. In the step response experiment, the load is 8 Ω resistive load, and the DC link voltage is 400V. It is estimated that the response time with the TE method is 1.6ms, while the one with the AAI method is 3ms, which demonstrates the good dynamic performance of the controller and the superiority of the TE over the AAI delay compensation method.

The level of distortion caused by a nonlinear load (a three-phase diode rectifier) is also a reflection of the control performance. Fig. 12 is the nonlinear load experimental results
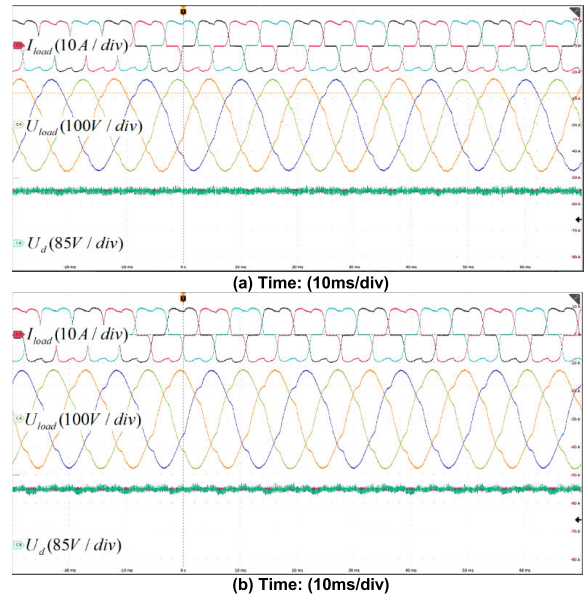

FIGURE 12. Nonlinear load-supporting performance of the LC filter-based converter: (a) with the TE method, (b) with the AAI method.
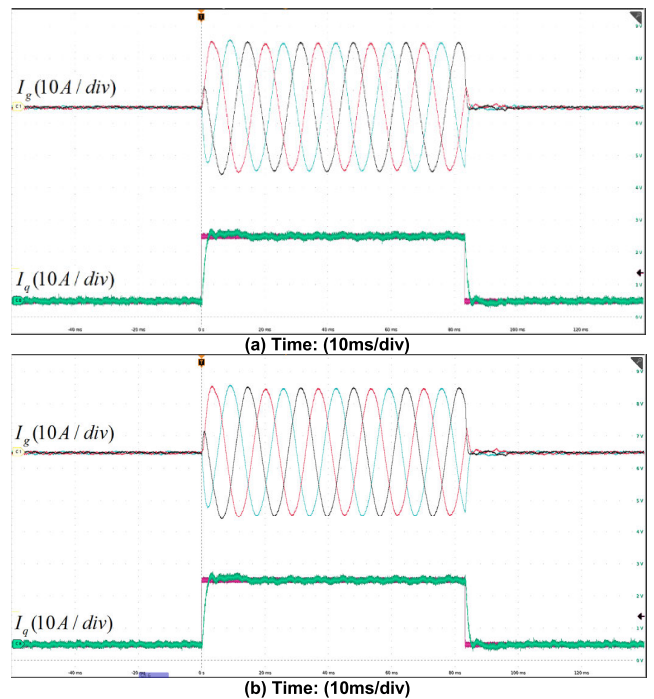

FIGURE 13. Step response of the LC filter-based converter: (a) with the TE (b) with AAI delay compensation method.

of the LC filter-based converter with the TE and AAI delay compensation methods respectively. From Fig.12(a), it can be found out that the load voltage is rather sinusoidal. The load voltage THD is measured to be 3.5%, which is acceptable in most applications. From Fig.12(b), it can be found out that the load voltage distortion with the AAI is higher than that with TE. The load voltage THD is measured to be 5.5%. According to IEEE Standard 519–2014, the acceptable limit is 5%. Therefore, it is not acceptable with the AAI method.

Fig.13 is the step response of the LCL filter-based converter with the TE and AAI delay compensation method.

From top to bottom, the two waveforms are grid current, reference, and measured current respectively. The converter is connected to the grid, the reference current is changed from 0 A to 20A periodically. From Fig.13(a), it is estimated that the step response time is 2.2ms, which demonstrates the good dynamic performance of the controller. The resonance exits in the form of harmonics. There is no current harmonic distortion, which demonstrates the good damping performance. From Fig.13(b), it is estimated the step response time is 2.3ms. The performance difference between the two delay compensation methods is insignificant. This is due to the significant phase shift introduced by the second-order derivative term with the GI differential method. The phase shift is twice as much as that of the first-order derivative term and has become the performance bottleneck of the controller. Therefore, the influence of delay compensation is insignificant in this situation. The analog differentiator can be used to break the bottleneck if better control performance is desired.

VII. CONCLUSION

A control bandwidth optimized AD control strategy for high order LC and LCL filter-based converter is proposed in this paper. With the proposed control strategy, an Nth order filter-based converter's closed-loop transfer function can be simplified into an Nth order low-pass filter. The dynamic performance can be tuned by adjusting the filter cutoff frequency. The steady-state performance can be tuned by adjusting the pole value which has been canceled in the closed-loop transfer function by the feedforward controller. The proposed control strategy is ideal for parameter optimization since both dynamic and steady-state performance can be both easily tuned.

The computational delay is the bottleneck that deteriorates the control performance. To alleviate the negative impact of the computational delay, a novel delay compensator with good delay compensation performance is proposed. To optimize the control and delay compensator parameters simultaneously, a PSO based global optimization scheme with a novel cost function is proposed.

The proposed approaches are implemented in an experimental platform. Experimental results verify the good performance of the proposed approaches.

REFERENCES

[1] Q. Liu, T. Caldognetto, and S. Buso, "Review and comparison of grid-tied inverter controllers in microgrids," *IEEE Trans. Power Electron.*, vol. 35, no. 7, pp. 7624–7639, Jul. 2020.

[2] W. Guo, D. Li, F. Cai, C. Zhao, and L. Xiao, "Z-source-converter-based power conditioning system for superconducting magnetic energy storage system," *IEEE Trans. Power Electron.*, vol. 34, no. 8, pp. 7863–7877, Aug. 2019.

[3] M. Wang, Y. Xu, and J. Zou, "Sliding mode control with open-switch fault diagnosis and sensorless estimation based on PI observer for PMSM drive connected with an LC filter," *IET Power Electron.*, vol. 13, no. 11, pp. 2334–2341, Aug. 2020.

[4] Q. Guo, C. Tu, F. Jiang, R. Zhu, and J. Gao, "Improved dual-functional DVR with integrated auxiliary capacitor for capacity optimization," *IEEE Trans. Ind. Electron.*, vol. 68, no. 10, pp. 9755–9766, Oct. 2021.

[5] M. F. Alsolami, K. A. Potty, and J. Wang, "Mitigation of double-line-frequency current ripple in switched capacitor based UPS system," *IEEE Trans. Power Electron.*, vol. 36, no. 4, pp. 4042–4051, Apr. 2021.

[6] R. Peña-Alzola, M. Liserre, F. Blaabjerg, R. Sebastián, J. Dannehl, and F. W. Fuchs, "Analysis of the passive damping losses in LCL-filter-based grid converters," *IEEE Trans. Power Electron.*, vol. 28, no. 6, pp. 2642–2646, Jun. 2013.

[7] W. Wu, Y. Sun, M. Huang, X. Wang, H. Wang, F. Blaabjerg, M. Liserre, and H. S.-H. Chung, "A robust passive damping method for LLCL-filter-based grid-tied inverters to minimize the effect of grid harmonic voltages," *IEEE Trans. Power Electron.*, vol. 29, no. 7, pp. 3279–3289, Jul. 2014.

[8] W. Tang, K. Ma, and Y. Song, "Critical damping ratio to ensure design efficiency and stability of LCL filters," *IEEE Trans. Power Electron.*, vol. 36, no. 1, pp. 315–325, Jan. 2021.

[9] J. W. He and Y. W. Li, "Generalized closed-loop control schemes with embedded virtual impedances for voltage source converters with LC or LCL filters," *IEEE Trans. Power Electron.*, vol. 27, no. 4, pp. 1850–1861, Apr. 2012.

[10] H.-C. Chen, P.-T. Cheng, F. Blaabjerg, and X. Wang, "A passivity-based stability analysis of the active damping technique in the offshore wind farm applications," *IEEE Trans. Ind. Appl.*, vol. 54, no. 5, pp. 5074–5082, Sep./Oct. 2018.

[11] Y. He, X. Wang, X. Ruan, D. Pan, X. Xu, and F. Liu, "Capacitor-current proportional-integral positive feedback active damping for LCL-type grid-connected inverter to achieve high robustness against grid impedance variation," *IEEE Trans. Power Electron.*, vol. 34, no. 12, pp. 12423–12436, Dec. 2019.

[12] L. Peng, W. Wu, and K. Hu, "A multicell network control and design for three-phase grid-connected inverter," *IEEE Trans. Ind. Electron.*, vol. 68, no. 4, pp. 2740–2749, Apr. 2021.

[13] J. Dannehl, F. W. Fuchs, S. Hansen, and P. B. Thøgersen, "Investigation of active damping approaches for PI-based current control of grid-connected pulse width modulation converters with LCL filters," *IEEE Trans. Ind. Appl.*, vol. 46, no. 4, pp. 1509–1517, Jul./Aug. 2010.

[14] R. Peña-Alzola, M. Liserre, F. Blaabjerg, R. Sebastián, J. Dannehl, and F. W. Fuchs, "Systematic design of the lead-lag network method for active damping in LCL-filter based three phase converters," *IEEE Trans. Ind. Informat.*, vol. 10, no. 1, pp. 43–52, Feb. 2014.

[15] L. Harnefors, A. G. Yepes, A. Vidal, and J. Doval-Gandoy, "Passivity-based controller design of grid-connected VSCs for prevention of electrical resonance instability," *IEEE Trans. Ind. Electron.*, vol. 62, no. 2, pp. 702–710, Feb. 2015.

[16] Z. Xin, X. Wang, P. C. Loh, and F. Blaabjerg, "Realization of digital differentiator using generalized integrator for power converters," *IEEE Trans. Power Electron.*, vol. 30, no. 12, pp. 6520–6523, Dec. 2015.

[17] Z. Xin, P. C. Loh, X. Wang, F. Blaabjerg, and Y. Tang, "Highly accurate derivatives for LCL-filtered grid converter with capacitor voltage active damping," *IEEE Trans. Power Electron.*, vol. 31, no. 5, pp. 3612–3625, May 2016.

[18] D. Pan, X. Ruan, and X. Wang, "Direct realization of digital differentiators in discrete domain for active damping of LCL-type grid-connected inverter," *IEEE Trans. Power Electron.*, vol. 33, no. 10, pp. 8461–8473, Oct. 2018.

[19] H. Zhang, X. Ruan, Z. Lin, L. Wu, Y. Ding, and Y. Guo, "Capacitor voltage full feedback scheme for LCL-type grid-connected inverter to suppress current distortion due to grid voltage harmonics," *IEEE Trans. Power Electron.*, vol. 36, no. 3, pp. 2996–3006, Mar. 2021.

[20] T. Liu, J. Liu, Z. Liu, and Z. Liu, "A study of virtual resistor-based active damping alternatives for LCL resonance in grid-connected voltage source inverters," *IEEE Trans. Power Electron.*, vol. 35, no. 1, pp. 247–262, Jan. 2020.

[21] W. Ma, Y. Guan, B. Zhang, and L. Wu, "Active disturbance rejection control based single current feedback resonance damping strategy for LCL-type grid-connected inverter," *IEEE Trans. Energy Convers.*, vol. 36, no. 1, pp. 48–62, Mar. 2021.

[22] L. Zhou, X. Zhou, Y. Chen, Z. Lv, Z. He, W. Wu, L. Yang, K. Yan, A. Luo, and J. M. Guerrero, "Inverter-current-feedback resonance-suppression method for LCL-type DG system to reduce resonance-frequency offset and grid-inductance effect," *IEEE Trans. Ind. Electron.*, vol. 65, no. 9, pp. 7036–7048, Sep. 2018.

[23] W. Chen, Y. Zhang, Y. Tu, K. Shen, and J. Liu, "Active damping control for LCL filters with inverter-side current feedback only," *IEEE Trans. Power Electron.*, vol. 37, no. 9, pp. 10065–10069, Sep. 2022.

[24] X. Li, J. Fang, Y. Tang, and X. Wu, "Robust design of LCL filters for single-current-loop-controlled grid-connected power converters with unit PCC voltage feedforward," *IEEE J. Emerg. Sel. Top. Power Electron.*, vol. 6, no. 1, pp. 54–72, Mar. 2018.

[25] Y. He, X. Wang, X. Ruan, D. Pan, and K. Qin, "Hybrid active damping combining capacitor current feedback and point of common coupling voltage feedforward for LCL-type grid-connected inverter," *IEEE Trans. Power Electron.*, vol. 36, no. 2, pp. 2373–2383, Feb. 2021.

[26] M. A. Awal, L. Della Flora, and I. Husain, "Observer based generalized active damping for voltage source converters with LCL filters," *IEEE Trans. Power Electron.*, vol. 37, no. 1, pp. 125–136, Jan. 2022.

[27] J. Zhao, C. Xie, K. Li, J. Zou, and J. M. Guerrero, "Passivity-oriented design of LCL-type grid-connected inverters with Luenberger observer-based active damping," *IEEE Trans. Power Electron.*, vol. 37, no. 3, pp. 2625–2635, Mar. 2022.

[28] C. Cheng, S. Xie, Q. Qian, J. Lv, and J. Xu, "Observer-based single-sensor control schemes for LCL-filtered grid-following inverters," *IEEE Trans. Ind. Electron.*, vol. 70, no. 5, pp. 4887–4900, May 2023, doi: 10.1109/TIE.2022.3189070.

[29] H. Liu, D. Xu, L. Li, and Q. Gao, "Robust damping method for voltage source converter with LCL-type filter under weak grid conditions," *CSEE J. Power Energy Syst.*, vol. 8, no. 5, pp. 1428–1437, Sep. 2022, doi: 10.17775/CSEEJPES.2019.02400.

[30] X. Chen, W. Wu, N. Gao, H. S.-H. Chung, M. Liserre, and F. Blaabjerg, "Finite control set model predictive control for LCL-filtered grid-tied inverter with minimum sensors," *IEEE Trans. Ind. Electron.*, vol. 67, no. 12, pp. 9980–9990, Dec. 2020.

[31] S. Bibian and H. Jin, "Time delay compensation of digital control for DC switchmode power supplies using prediction techniques," *IEEE Trans. Power Electron.*, vol. 15, no. 5, pp. 835–842, Sep. 2000.

[32] X. Li, X. Wu, Y. Geng, X. Yuan, C. Xia, and X. Zhang, "Wide damping region for LCL-type grid-connected inverter with an improved capacitor-current-feedback method," *IEEE Trans. Power Electron.*, vol. 30, no. 9, pp. 5247–5259, Sep. 2015.

[33] C. Chen, J. Xiong, Z. Wan, J. Lei, and K. Zhang, "A time delay compensation method based on area equivalence for active damping of an LCL-type converter," *IEEE Trans. Power Electron.*, vol. 32, no. 1, pp. 762–772, Jan. 2017.

[34] Z. Xin, X. Wang, P. C. Loh, and F. Blaabjerg, "Grid-current-feedback control for LCL-filtered grid converters with enhanced stability," *IEEE Trans. Power Electron.*, vol. 32, no. 4, pp. 3216–3228, Apr. 2017.

[35] M. Lu, X. Wang, P. C. Loh, F. Blaabjerg, and T. Dragicevic, "Graphical evaluation of time-delay compensation techniques for digitally controlled converters," *IEEE Trans. Power Electron.*, vol. 33, no. 3, pp. 2601–2614, Mar. 2018.

[36] H. Zhang, X. Wang, Y. He, D. Pan, and X. Ruan, "A compensation method to eliminate the impact of time delay on capacitor-current active damping," *IEEE Trans. Ind. Electron.*, vol. 69, no. 7, pp. 7512–7516, Jul. 2022.

WENYONG GUO (Member, IEEE) received the B.E. degree in automation from Beihang University (formerly BUAA), Beijing, China, in 2002, and the Ph.D. degree in electrical engineering from the University of Chinese Academy of Sciences, Beijing, in 2008.

From 2008 to 2022, he was with the Institute of Electrical Engineering, Chinese Academy of Sciences, where he was also a Professor, in 2016. He is currently a Professor with Beijing Jiaotong University. His research interests include wind turbine control, energy storage, and fault current limiter.

TIANXIANG CHEN (Member, IEEE) was born in Hangzhou, China. He received the B.Eng. degree in electrical engineering from the Harbin Institute of Technology, Harbin, China, in 2015, the M.S. degree in electrical engineering from North Carolina State University, Raleigh, NC, USA, in 2017, and the Ph.D. degree in electrical engineering from the Semiconductor Power Electronics Center, The University of Texas at Austin, Austin, TX, USA, in 2022. His research interests include the design, control, and optimization of high-density and high-frequency power converters.

ALEX Q. HUANG (Fellow, IEEE) was born in Zunyi, Guizhou, China. He received the B.Sc. degree in electrical engineering from Zhejiang University, Hangzhou, China, in 1983, the M.Sc. degree in electrical engineering from the Chengdu Institute of Radio Engineering, Chengdu, China, in 1986, and the Ph.D. degree in electrical engineering from the University of Cambridge, Cambridge, U.K., in 1992.

From 1992 to 1994, he was a Research Fellow with the Magdalene College, Cambridge, U.K. From 1994 to 2004, he was a Professor with The Bradley Department of Electrical and Computer Engineering, Virginia Polytechnic Institute and State University, Blacksburg, VA, USA. From 2004 to 2017, he was the Progress Energy Distinguished Professor of electrical and computer engineering with North Carolina State University, Raleigh, NC, USA, where he established and led the NSF FREEDM Systems Center. Since 2017, he has been the Dula D. Cockrell Centennial Chair of Engineering with The University of Texas at Austin. Since 1983, he has also been involved in the development of modern power semiconductor devices and power integrated circuits. He fabricated the first insulated-gate bipolar transistor (IGBT) power device in China, in 1985. He is the inventor and a key developer of the emitter turn-off (ETO) thyristor. He developed the concept of energy internet and the smart transformer-based energy router technology. He has mentored and graduated more than 80 Ph.D. and master's students. He has published more than 500 papers in international conferences and journals. He has also been granted more than 20 U.S. patents. His current research interests include power electronics, power management microsystems, and power semiconductor devices.

Dr. Huang is a fellow of the National Academy of Inventors. He was a recipient of the NSF CAREER Award, the prestigious Research and Development 100 Award, the MIT Technology Review's 2011 Technology of the Year Award, and the 2019 IEEE IAS Gerald Kliman Innovator Award.

● ● ●